Plant Communications
Research article

CellPress
Partner Journal

Structural insights into brassinosteroid export mediated by the *Arabidopsis* ABC transporter ABCB1

Hong Wei[1,7], Heyuan Zhu[2,3,7], Wei Ying[1,7], Hilde Janssens[4], Miroslav Kvasnica[5], Johan M. Winne[4], Yongxiang Gao[1], Jiří Friml[6], Qian Ma[2,3], Shutang Tan[1,*], Xin Liu[1,*], Eugenia Russinova[2,3,*] and Linfeng Sun[1,*]

[1]MOE Key Laboratory for Membraneless Organelles and Cellular Dynamics, Hefei National Research Center for Physical Sciences at the Microscale, Center for Advanced Interdisciplinary Science and Biomedicine of IHM, Division of Life Sciences and Medicine, University of Science and Technology of China, Hefei 230027, China

[2]University Department of Plant Biotechnology and Bioinformatics, Ghent University, 9052 Ghent, Belgium

[3]Center for Plant Systems Biology, VIB, 9052 Ghent, Belgium

[4]Department of Organic and Macromolecular Chemistry, Ghent University, 9000 Ghent, Belgium

[5]Laboratory of Growth Regulators, Institute of Experimental Botany, The Czech Academy of Sciences and Palacký University, 77900 Olomouc, Czech Republic

[6]Institute of Science and Technology Austria (ISTA), Am Campus 1, 3400 Klosterneuburg, Austria

[7]These authors contributed equally to this article.

***Correspondence: Shutang Tan (sttan@ustc.edu.cn), Xin Liu (lx023@ustc.edu.cn), Eugenia Russinova (eugenia.russinova@psb.vib-ugent.be), Linfeng Sun (sunlf17@ustc.edu.cn)**

https://doi.org/10.1016/j.xplc.2024.101181

ABSTRACT

Brassinosteroids (BRs) are steroidal phytohormones indispensable for plant growth, development, and responses to environmental stresses. The export of bioactive BRs to the apoplast is essential for BR signaling initiation, which requires binding of a BR molecule to the extracellular domains of the plasma membrane–localized receptor complex. We have previously shown that the *Arabidopsis thaliana* ATP-binding cassette (ABC) transporter ABCB19 functions as a BR exporter and, together with its close homolog ABCB1, positively regulates BR signaling. Here, we demonstrate that ABCB1 is another BR transporter. The ATP hydrolysis activity of ABCB1 can be stimulated by bioactive BRs, and its transport activity was confirmed in proteoliposomes and protoplasts. Structures of ABCB1 were determined in substrate-unbound (apo), brassinolide (BL)-bound, and ATP plus BL-bound states. In the BL-bound structure, BL is bound to the hydrophobic cavity formed by the transmembrane domain and triggers local conformational changes. Together, our data provide additional insights into ABC transporter–mediated BR export.

Key words: brassinosteroids, ABCB1, *Arabidopsis*, structure, transport, signaling

Wei H., Zhu H., Ying W., Janssens H., Kvasnica M., Winne J.M., Gao Y., Friml J., Ma Q., Tan S., Liu X., Russinova E., and Sun L. (2025). Structural insights into brassinosteroid export mediated by the *Arabidopsis* ABC transporter ABCB1. Plant Comm. **6**, 101181.

INTRODUCTION

As the only steroidal hormones in plants, brassinosteroids (BRs) regulate a plethora of physiological and developmental processes (Nolan et al., 2020). BR signaling is initiated by binding of the bioactive BR molecule to the extracellular domains of the membrane-embedded receptor complex (Fujioka and Yokota, 2003; Hothorn et al., 2011; She et al., 2011; Santiago et al., 2013; Sun et al., 2013; Northey et al., 2016). However, BRs are synthesized in the cell interior by enzymes localized in the endoplasmic reticulum membrane (Kim et al., 2006; Northey et al., 2016; Wang et al., 2023). Hence, the membrane permeation of BRs is essential for initiation of the signaling cascade. As BR biosynthesis proceeds, the steroidal precursors undergo polyhydroxylation, thus making the bioactive BRs more polar (Choe et al., 1998; Fujioka and Yokota, 2003; Vukasinovic and Russinova, 2018). Molecular

Published by the Plant Communications Shanghai Editorial Office in association with Cell Press, an imprint of Elsevier Inc., on behalf of CSPB and CEMPS, CAS.

dynamic simulations indicate that it is difficult for steroidal molecules with polyhydroxyl groups to diffuse through the membrane (Atkovska et al., 2018), implying that BR exporters are needed in this process. Although BRs do not undergo long-distance transport, their short-distance movement is important for BR biosynthesis and signaling (Symons and Reid, 2004; Vukasinovic and Russinova, 2018; Vukasinovic et al., 2021; Wang et al., 2023).

ABCB1 (or P-glycoprotein 1 [PGP1]) and ABCB19 (or multidrug resistance 1 [MDR1]) are the first two members of the multidrug resistance (MDR)-family ABC transporters identified in *Arabidopsis thaliana* (*Arabidopsis*) (Dudler and Hertig, 1992; Noh et al., 2001; Sánchez-Fernández et al., 2001; Rea, 2007) and share a sequence identity of 53% (Supplemental Figure 1). In contrast to the dwarf *abcb19* mutant, the *abcb1* mutant exhibits no significant phenotypic changes under long-day growth conditions but displays a less severe dwarf phenotype when grown in short-day conditions (Noh et al., 2001, 2003; Geisler et al., 2005; Lin and Wang, 2005; Ye et al., 2013). ABCB1 and ABCB19 were originally characterized as auxin exporters (Noh et al., 2001, 2003; Geisler et al., 2005; Lin and Wang, 2005; Lewis et al., 2007; Hao et al., 2020). The expression of both proteins is auxin responsive (Noh et al., 2001; Geisler et al., 2005), and the basipetal movement of auxin in inflorescence stems and seedlings was reduced in the *abcb19* mutant, exaggerated in the *abcb1 abcb19* double mutant, but not compromised in the *abcb1* mutant (Noh et al., 2001). Auxin efflux activities of ABCB1 and ABCB19 have been demonstrated by either the reduced indole-3-acetic acid (IAA) export in *Arabidopsis* protoplasts isolated from *abcb1*, *abcb19*, and *abcb1 abcb19* mutants or the increased IAA export in heterologous systems, including yeast and HeLa cells, overexpressing ABCB1 or ABCB19 (Geisler et al., 2005; Bouchard et al., 2006; Bailly et al., 2008; Henrichs et al., 2012; Hao et al., 2020). Recently, we have shown that *Arabidopsis* ABCB19 exports bioactive BRs and positively regulates BR signaling together with its close homolog ABCB1 (Ying et al., 2024). However, whether ABCB1 is also a BR transporter awaits validation.

In this study, we showed that, like ABCB19, *Arabidopsis* ABCB1 can also export bioactive BRs, as supported by *in vitro* ATPase activity measurements, as well as proteoliposome-based and *in planta* protoplast-based transport assays. High-resolution structures were determined for ABCB1 in three different states using cryo-electron microscopy (cryo-EM) single-particle analysis. Conformational changes were observed in the transmembrane domains of ABCB1 upon BR binding, further revealing how the bioactive BR molecule is recognized by ABCB1 and the dynamics of BR export.

RESULTS

ABCB1 can export bioactive BRs

To test whether ABCB1 is a BR transporter, we first purified *Arabidopsis* ABCB1 using the human embryonic kidney 293F (HEK293F) cell expression system. Like that of ABCB19 (Ying et al., 2024), the protein yield of ABCB1 was only improved when co-expressed with the immunophilin-like protein TWISTED DWARF1 (TWD1) (Supplemental Figure 2A), providing evidence that TWD1 functions as a molecular chaperone of ABCB1 and ABCB19 (Yin et al., 2002; Wu et al., 2010). We then tested the ATPase activity of ABCB1 in the presence of four different phytohormones: two natural auxins (IAA and indole 3-butyric acid [IBA]), brassinolide (BL), and gibberellic acid-3 (GA3) (Figure 1A). The ATPase activity of ABCB1 was dramatically increased by BL but not by the auxins or GA3. The V_{max} value of dose-dependent stimulation by BL was 215.5 ± 3.9 $nmol^{-1}$ min^{-1} mg^{-1} protein using the Hill equation (*n* value prefixed to 1.0), and the half maximal effective concentration (EC_{50}) was 0.69 ± 0.09 μM (Figure 1A). Such stimulations were also observed under different ATP concentrations, comparing the ATPase activities of wild-type ABCB1 ($ABCB1^{WT}$) in the presence or absence of BL (Supplemental Figure 2B). The ABCB1 catalytic mutant ($ABCB1^{EQ}$), in which two conserved glutamates (E532 and E1188) in the Walker-B motif of the nucleotide-binding domains (NBDs) were mutated to glutamines, served as a control and showed no ATPase activity in the presence or absence of BL (Supplemental Figure 2B). ATPase activity was also inhibited by the potent inhibitor vanadate in the presence or absence of BL (Supplemental Figure 2C). In addition to BL, two other bioactive BRs, 24-epibrassinolide (24-epiBL) and 24-epicastasterone (24-epiCS), also increased the ATPase activity of ABCB1 (Figure 1B), but the less-hydroxylated BR precursors campesterol and 22-hydroxycampesterol (22-OHCR) and the mammalian steroids cholesterol, taurocholic acid, and estrone sulfate did not (Figure 1B). We compared the ATPase activities of ABCB1 and ABCB19 under the same assay conditions. The results showed that the ATPase activity at a given concentration of BL or the V_{max} value of ABCB1 was much higher than that of ABCB19 (Figure 1C and 1D), whereas the EC_{50} values of ABCB1 for BL, 24-epiBL, or 24-epiCS were similar to those reported for ABCB19 (Figure 1D) (Ying et al., 2024). The BL-triggered ATPase activity of ABCB1 was unaffected by the presence of auxins such as IAA or IBA (Supplemental Figure 2D and 2E), suggesting that auxin might not compete for the BL-binding site of ABCB1.

To test the BR transport activity of ABCB1, we first used the proteoliposome-based transport assay described previously for ABCB19 (Ying et al., 2024). Purified ABCB1 proteins were reconstituted into proteoliposomes. Accumulation of [^{3}H]-labeled BL ([^{3}H]-BL) in proteoliposomes was determined for $ABCB1^{WT}$ or the catalytic $ABCB1^{EQ}$ mutant in reaction buffer with or without the ATPase inhibitor vanadate. [^{3}H]-BL accumulation was greater for proteoliposomes loaded with $ABCB1^{WT}$ in reaction buffer without vanadate than for those tested in buffer with vanadate or those loaded with the EQ mutant (Figure 1E), suggesting that ABCB1 can transport bioactive BR *in vitro* using the energy of ATP hydrolysis. No active transport of IAA or IBA was detected in this proteoliposome-based assay system (Supplemental Figure 2F and 2G), as also reported for ABCB19 (Ying et al., 2024). However, in a cell-based auxin-loading assay, cells expressing both ABCB1 and TWD1 accumulated less [^{3}H]-IAA than those expressing TWD1 alone (Supplemental Figure 2H), suggesting an active auxin efflux activity of ABCB1 under *in vivo* conditions, similar to that of ABCB19 (Ying et al., 2024). We then tested the BR transport activity of ABCB1 in *Arabidopsis* protoplasts using the bioactive clickable BL precursor castasterone (CS)-alkyne (CSA). Similar to BL, CSA also triggered the ATPase activity of ABCB1, although less potently, with a V_{max}

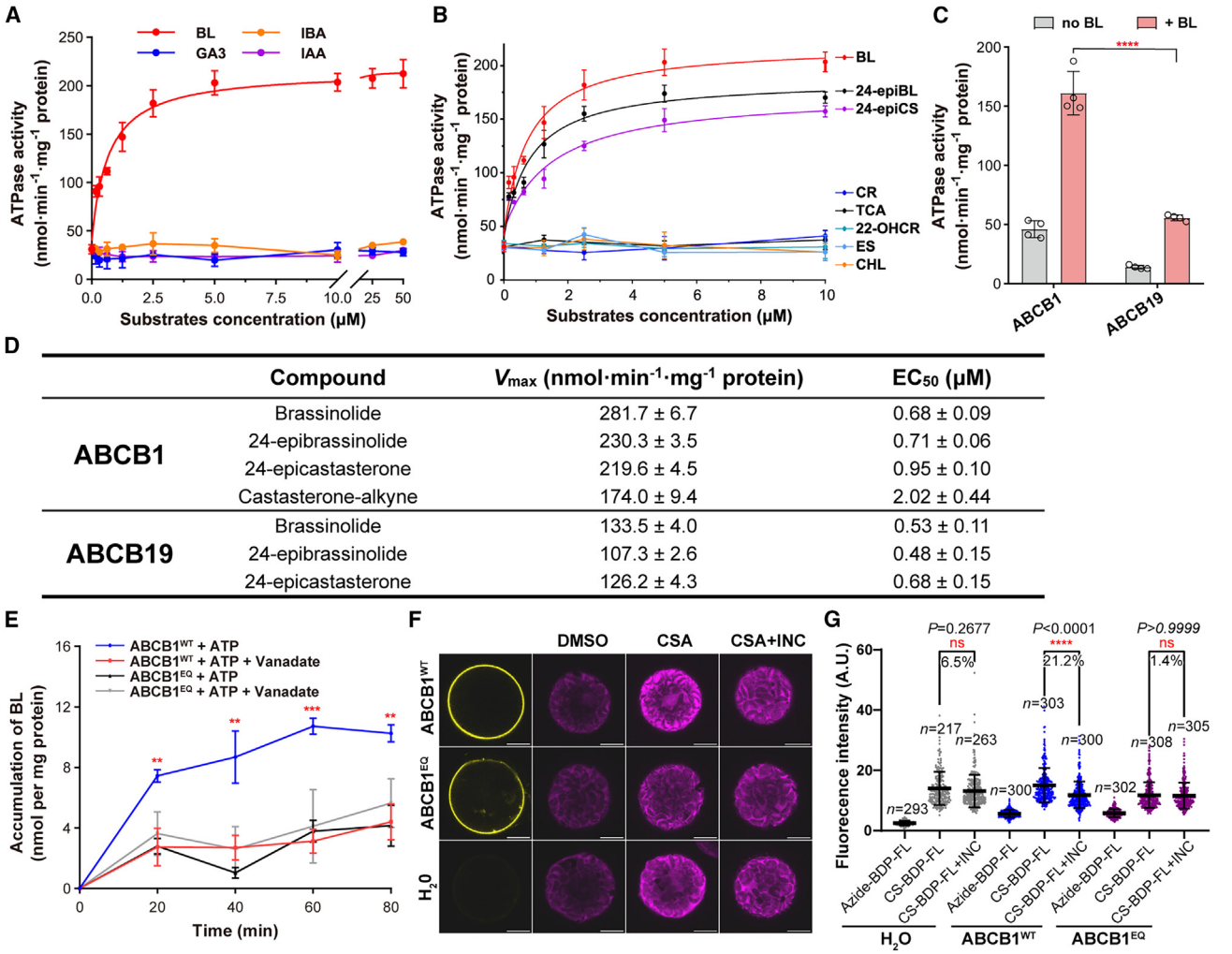

	Compound	V_{max} (nmol·min^{-1}·mg^{-1} protein)	EC_{50} (μM)
ABCB1	Brassinolide	281.7 ± 6.7	0.68 ± 0.09
	24-epibrassinolide	230.3 ± 3.5	0.71 ± 0.06
	24-epicastasterone	219.6 ± 4.5	0.95 ± 0.10
	Castasterone-alkyne	174.0 ± 9.4	2.02 ± 0.44
ABCB19	Brassinolide	133.5 ± 4.0	0.53 ± 0.11
	24-epibrassinolide	107.3 ± 2.6	0.48 ± 0.15
	24-epicastasterone	126.2 ± 4.3	0.68 ± 0.15

Figure 1. ABCB1 transports BRs.

(A) ATPase activity of ABCB1 in the presence of different phytohormones, including indole-3-acetic acid (IAA), indole 3-butyric acid (IBA), gibberellic acid-3 (GA3), and brassinolide (BL).

(B) Steroid-concentration-dependent ATPase activity of ABCB1.

(C) ATPase activities of ABCB1 and ABCB19 in the presence or absence of 5 μM BL. Significance was determined using an unpaired *t*-test. ****$p < 0.0001$. Data in **(B)** and **(C)** are means of four independent measurements ±SD.

(D) Comparisons of kinetic parameters of the ATPase activity of ABCB1 and those previously reported for ABCB19.

(E) Accumulation of BL was higher in ABCB1^{WT}-loaded proteoliposomes in buffer with 2 mM ATP than in buffer with ATP and vanadate and in ABCB1^{EQ} mutant-loaded proteoliposomes. Significant differences between ABCB1^{WT} proteoliposomes with or without vanadate were determined using an unpaired *t*-test. **$p < 0.0021$, ***$p = 0.0002$. Data in **(A)** and **(E)** are means of three independent measurements ±SD.

(F) The export of castasterone-alkyne (CSA) was increased in *Arabidopsis* protoplasts expressing ABCB1^{WT}-GFP but not in protoplasts expressing ABCB1^{EQ}-GFP, as detected by a bioorthogonal chemistry-based transport assay. The signal is shown after the bioorthogonal reaction with azide-BDP-FL. Scale bars, 10 μm.

(G) Quantification of the fluorescence intensity shown in **(F)**. All individual data points are plotted. Black horizontal bars represent the means, and error bars represent SD. The percentage shows the reduction in CS-BDP-FL signal after incubation (INC). *n*, number of cells analyzed. A.U., arbitrary units. Significant differences were determined by one-way ANOVA with Tukey's multiple comparison test. ****$p < 0.0001$. ns, not significant. **(F and G)** The experiment was repeated independently twice with similar results, and one representative experiment is shown.

value of 174.0 ± 9.4 nmol^{-1} min^{-1} mg^{-1} protein and an EC_{50} of 2.02 ± 0.44 μM (Figure 1D and Supplemental Figure 2I), suggesting that ABCB1 can transport CSA, though less efficiently than BL (Supplemental Figure 2I). CSA was visualized after a click reaction with azide-BODIPY-fluorescein (azide-BDP-FL) (Figure 1F and 1G). When compared with non-transfected protoplasts or protoplasts expressing the ABCB1^{EQ}-GFP mutant or the *Arabidopsis* abscisic acid transporter GFP-ABCG25 (Kuromori et al., 2010; Huang et al., 2023; Ying et al., 2023), protoplasts expressing ABCB1^{WT}-GFP showed enhanced export of CSA (Figure 1F and 1G; Supplemental Figure 3A and 3B). The export efficiency of ABCB1^{WT}-GFP was comparable to that of ABCB19^{WT}-GFP, albeit consistently slightly weaker (Supplemental Figure 3A and 3B). In agreement with this result, CSA uptake was lower in protoplasts isolated from *abcb1* and *abcb1 abcb19* mutants than in those isolated from wild-type or

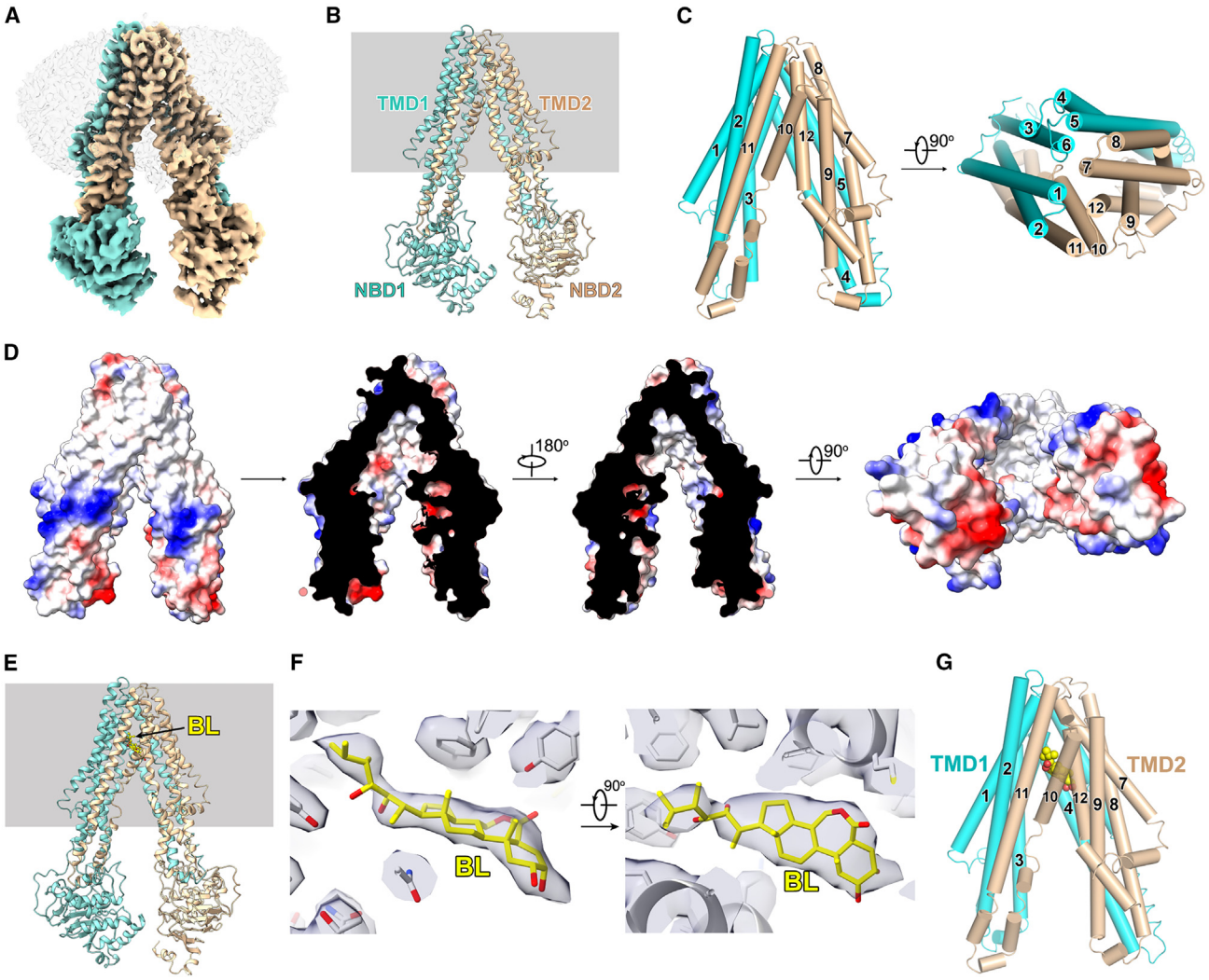

Figure 2. ABCB1 structures in the substrate-unbound and BL-bound states.

(A) Overview of the EM density map of ABCB1^{WT} in the substrate-unbound state. Transmembrane domain 1 (TMD1) and nucleotide-binding domain 1 (NBD1) are colored cyan. TMD2 and NBD2 are colored khaki.

(B) ABCB1 structure in the substrate-unbound state.

(C) A cartoon representation of the TMDs of ABCB1 in the substrate-unbound state.

(D) Overview of the surface electrostatic potential of the substrate-unbound ABCB1 structure.

(E) ABCB1^{WT} structure in the BL-bound state. The BL molecule is shown in sticks with carbon atoms colored yellow.

(F) EM density of the BL molecule shown by UCSF Chimera at a threshold of 0.8.

(G) The TMDs of ABCB1^{WT} in the BL-bound state. BL is shown in spheres.

p35S:ABCB1-GFP-expressing plants (Supplemental Figure 3C and 3D). Taken together, our data provide evidence that *Arabidopsis* ABCB1 is also a BR transporter.

Structural characterization of ABCB1 under different states

We next determined the structures of ABCB1 under different states. We co-expressed ABCB1^{WT} with TWD1 and purified the protein using the detergent digitonin (Supplemental Figure 4A). Using cryo-EM analysis, we obtained a density map for substrate-unbound ABCB1 at an overall resolution of 3.5 Å (Figure 2A, Supplemental Figures 4B–4F and 5A and 5B). By adding BL to the protein prior to cryo-sample preparation, we obtained an electron microscopy (EM) density map of BL-bound ABCB1^{WT} at a 3.5-Å resolution (Supplemental Figures 4G–4K and 6A and 6B). A clear density was identified in the cavity formed by the transmembrane domains (TMDs) and docked well with a BL molecule (Figure 2F). We also determined an EM map of the ABCB1^{EQ} mutant in the presence of both ATP and BL at an overall resolution of 3.8 Å (Supplemental Figure 7A–7G). Atomic models were built for ABCB1 under the three different states (Supplemental Table 1).

Architecture of ABCB1 in the apo and BL-bound states

The ABCB1 structure in the apo state exhibited a V-shaped architecture and adopted a conserved fold of the type-IV ABC transporters (Thomas et al., 2020; Thomas and Tampé, 2020; Alam and Locher, 2023) (Figure 2A and 2B). The amino

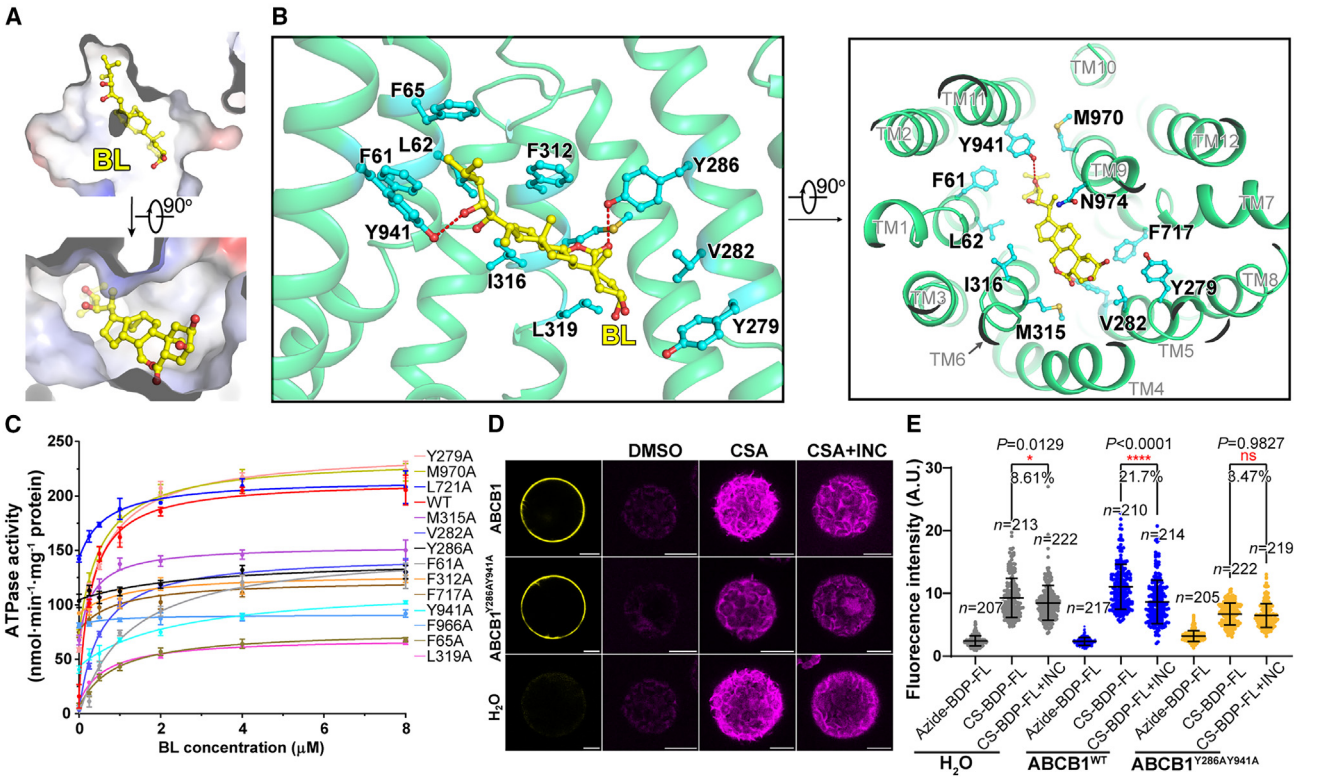

Figure 3. Coordination of BL by ABCB1.

(A) BL binds to a hydrophobic pocket of ABCB1. BL is shown in sticks.

(B) Zoomed-in views of the BL-bound structure of ABCB1^{WT}. BL is shown in sticks with carbon atoms colored yellow. Side chains of the residues close to BL are shown in sticks with carbon atoms colored cyan.

(C) BL-concentration-dependent ATPase activities of ABCB1^{WT} and its mutants. Data are fitted using the Hill equation. Data are means of three independent measurements ±SD.

(D) CSA export was reduced in *Arabidopsis* protoplasts overexpressing ABCB1^{Y286AY941A}-GFP. The signal is shown after bioorthogonal reaction with azide-BDP-FL. Scale bars, 10 μm.

(E) Quantification of the fluorescence intensity shown in **(D)**. All individual data points are plotted. Black horizontal bars represent the means, and error bars represent SDs. The percentage shows the reduction in CS-BDP-FL signal after incubation (INC). *n*, number of cells analyzed. A.U., arbitrary units. Significant differences were determined by one-way ANOVA with Tukey's multiple comparison test. *$p < 0.05$, ****$p < 0.0001$. ns, not significant. The experiment was performed once.

(N)-terminal and carboxyl (C)-terminal halves formed an inverted pseudo-dimer (Figure 2B). The two TMDs were arranged in a domain-swapped manner (Figure 2C) and formed a large cavity opening to the cytosol (Figure 2D). Thus, the determined substrate-unbound ABCB1 structure was in an inward-facing conformation, similar to that of ABCB19 (Ying et al., 2024). The surface of the cavity was mainly hydrophobic, favoring binding of hydrophobic molecules (Figure 2D).

In the BL-bound structure of ABCB1, the BL molecule was positioned in the bottom of a cytosolic-facing cavity (Figure 2E and 2G). F61, L62, F65 in transmembrane segment 1 (TM1), Y941 in TM11, and F966, M967, M970, and V971 in TM12 formed a cavity accommodating the polymethyl and polyhydroxyl side chain of BL (Figure 3A and 3B). The steroidal rings of BL bound to a hydrophobic surface formed by surrounding residues, including V282, Y286, F312, I316, L319, F717, and L721 (Figure 3B). In addition to hydrophobic interactions, Y941 formed a hydrogen bond with the hydroxyl group on C-23 (Figure 3B), and Y286 formed a hydrogen bond with the carbonyl oxygen of the ester group in the 7-oxalactone ring of BL (Figure 3B). Notably, the moieties of BL that formed hydrogen bonds with ABCB1 were absent in the biosynthetic precursors campesterol and 22-OHCR but were conserved in bioactive CS (Supplemental Figure 2J). This may explain why only bioactive BRs, and not their precursors, triggered the ATPase activity of ABCB1. We mutated each BL-binding residue into alanine and tested the ATPase and BL transport activities of the respective mutants (Figure 3C; Supplemental Figure 8A; Supplemental Table 2). Most mutants had lower ATPase activities than ABCB1^{WT} in the presence of the same BL concentrations (Figure 3C), with lower V_{max} values and greater EC_{50} values (Supplemental Table 2). Consistent with their lower ATPase activities, the BL-binding mutants also showed reduced BL transport activities in the proteoliposome-based transport assay compared with ABCB1^{WT} (Supplemental Figure 8A). The ABCB1^{Y279A} mutant, which was not affected in ATPase activity, was used as a control and displayed a wild-type BL transport ability (Figure 3C; Supplemental Figure 8A). ATPase and BL transport activities were reduced in the Y286A and Y941A single mutants, as well as the Y286A/Y941A double mutant (Supplemental

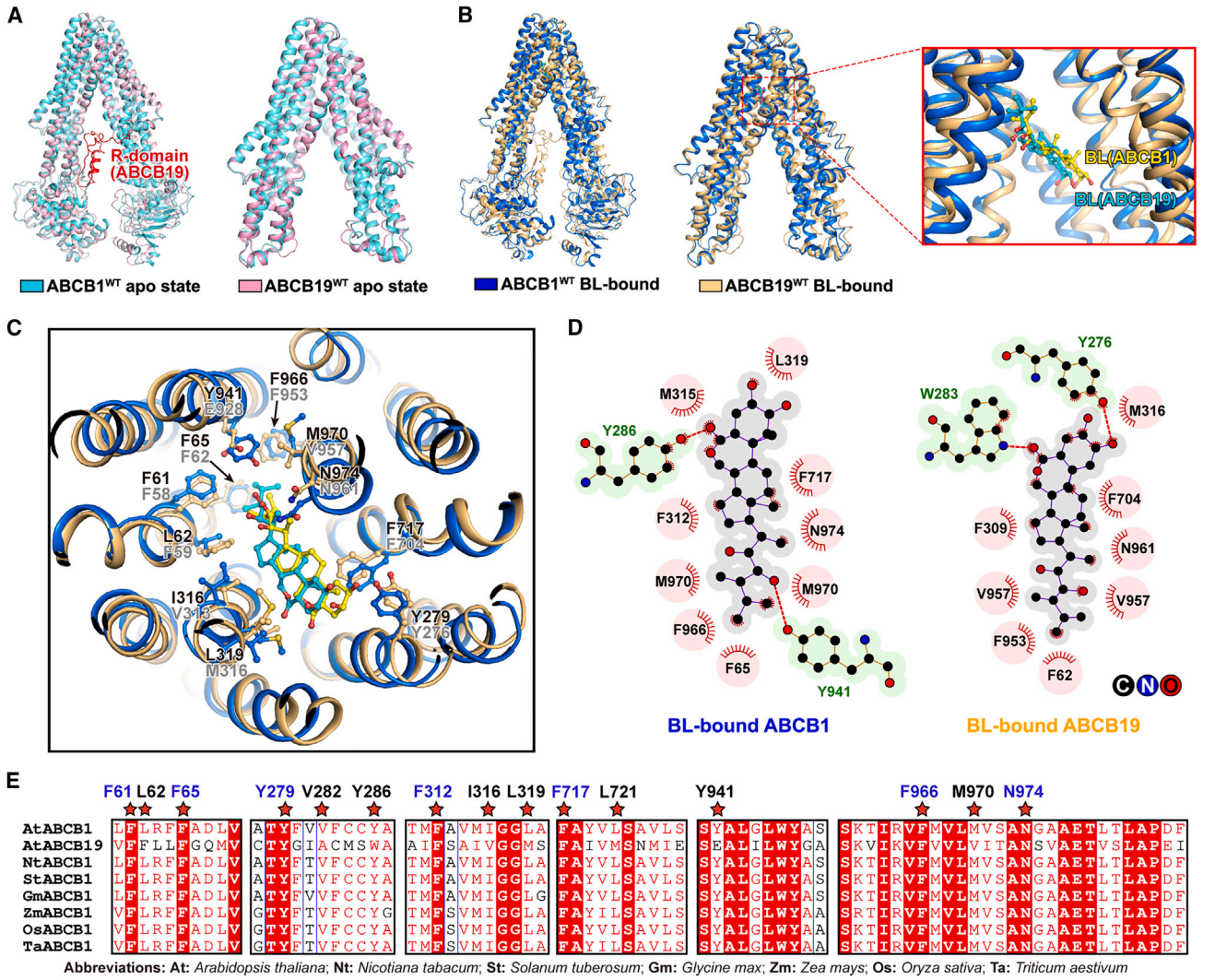

Figure 4. Structural comparisons between ABCB1 and ABCB19.

(A) Structure alignment of ABCB1 and ABCB19 (PDB: 8WOI) in the apo state.

(B) Structure alignment of ABCB1 and ABCB19 (PDB: 8WOM) in BL-bound state. A zoomed-in view of the BL-binding pocket is shown on the right.

(C) Structural comparison of the BL-binding site in ABCB1 and ABCB19. The color scheme is the same as that in **(B)**.

(D) Schematic representation of the interactions between BL and ABCB1 or ABCB19 as shown by Ligplot+ (red dashed lines, hydrogen bonds; spokes, hydrophobic interactions).

(E) Sequence alignment of *A. thaliana* ABCB1 with *A. thaliana* ABCB19 and ABCB1s from other representative plant species. Residues involved in BL binding in *A. thaliana* ABCB1 are marked at the top of the sequence. Invariant amino acids in all species are colored blue.

Figure 8A, 8B, and 8D). Consistent with this result, CSA export was reduced in protoplasts expressing ABCB1^{Y286A}-GFP, ABCB1^{Y941A}-GFP, or ABCB1^{Y286AY941A}-GFP (Figure 3D and 3E; Supplemental Figure 8F and 8G).

Structural comparisons between ABCB1 and ABCB19

Structural alignments of ABCB1 and ABCB19 in the apo state revealed a similar architecture with a root-mean-square deviation (RMSD) of 1.9 Å (1051 Cα atoms aligned) (Figure 4A). The TMDs of ABCB1 and ABCB19 merged well, except for shifts in the cytosolic portions of TM3, TM4, and TM9 (Supplemental Figure 9A). In the ABCB19 structures, an extra regulatory (R) domain was observed, formed by the linker between NBD1 and TMD2 that may be involved in regulating the transport activity of ABCB19 (Ying et al., 2024) (Figure 4A). However, we did not observe such a structure in ABCB1. In addition, the R-domain sequence in ABCB19 and the corresponding linker sequence in ABCB1 shared low similarities (Supplemental Figure 1). Whether the activity of ABCB1 is regulated through this sequence awaits further investigation.

BL bound to a conserved site in ABCB1 and ABCB19, as demonstrated by sequence and structural alignments (Figure 4B–4D; Supplemental Figure 1). The BL molecule used almost identical conformations in the two structures, with the steroidal rings packing to a hydrophobic surface and the polymethyl and polyhydroxyl side chain protruding into a hydrophobic pocket (Figure 4C and 4D). The interacting residues were highly conserved or invariant in ABCB1 and ABCB19 (Figure 4C–4E). However, some variations were observed, especially for the

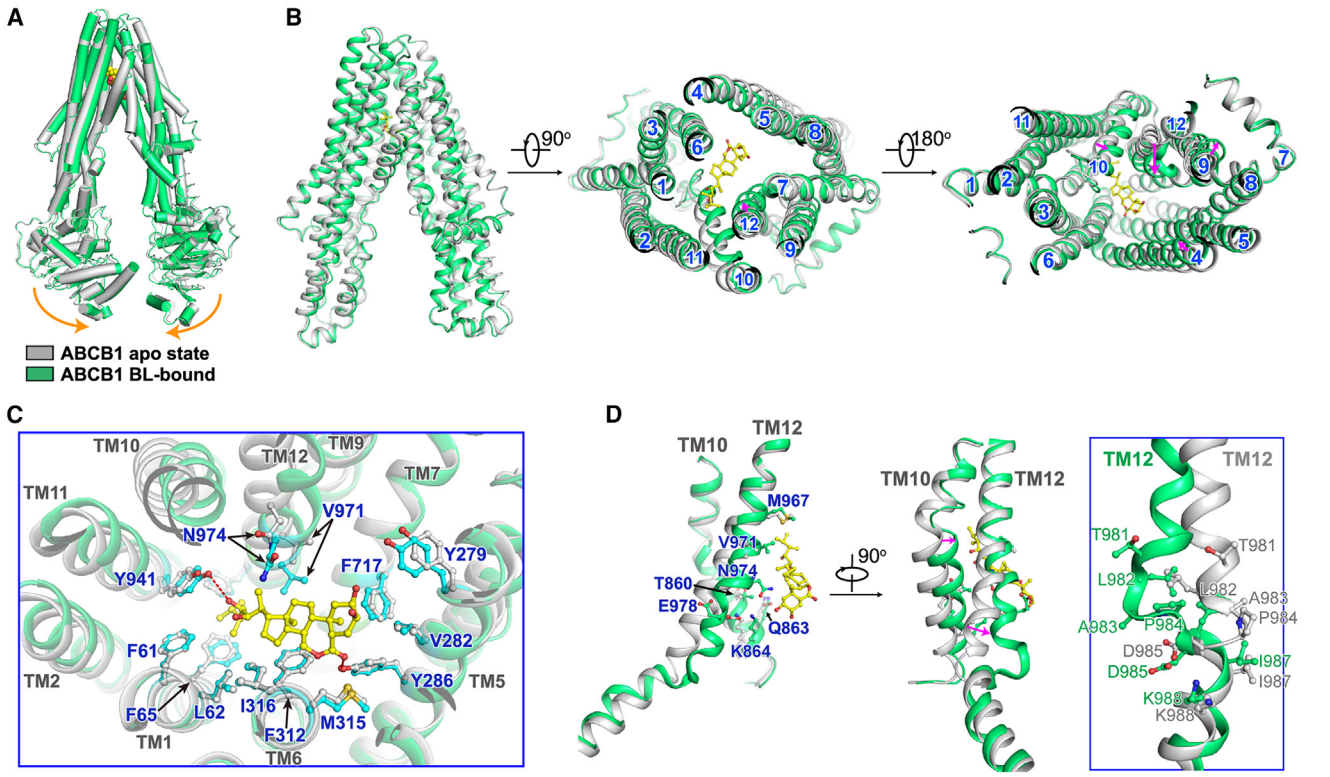

Figure 5. Structural changes in ABCB1 upon BL binding.

(A) Structure alignments of ABCB1 in the apo state (colored gray) and BL-bound state (colored green).

(B) Structure alignments of the TMDs of ABCB1 in the apo state and BL-bound state. Structural shifts are observed in TM4, TM9, TM10, and TM12, as indicated by magenta arrows.

(C) Structural comparison of the residues involved in BL binding in the apo-state structure (cartoon structure and carbon atoms colored gray) and BL-bound structure (cartoon structure and carbon atoms colored green and cyan) of ABCB1.

(D) Magnified views of the structural changes in TM10 and TM12 upon BL binding. BL is shown in sticks with carbon atoms colored yellow. Side chains of the residues adjacent to BL are shown in sticks. A magnified view of the structural changes in TM12 is shown in the blue box.

two residues that formed hydrogen bonds with BL in ABCB1, Y286 and Y941. In ABCB19, Y286 was substituted by a tryptophan residue (W283), and Y941 was replaced by a glutamate residue (E928) (Figure 4D and 4E; Supplemental Figure 1). In the BL-bound ABCB19 structure, no hydrogen bond was observed between E928 and BL, whereas W283 still formed a hydrogen bond with the carbonyl oxygen in the 7-oxalactone ring of BL (Rohou and Grigorieff, 2015). Together, these observations further supported the notion that the oxalactone moiety formed during the synthesis of active BRs plays a critical role in their binding to both ABCB1 and ABCB19. In addition to ABCB19, we also aligned the ABCB1 proteins from *Arabidopsis* and other plant species, including tobacco, potato, soybean, maize, rice, and wheat (Figure 4E; Supplemental Figure 10). They shared high sequence identity, about 75%–88% (Supplemental Figure 10), and the BL-binding residues were highly conserved and all invariant in the compared ABCB1s, suggesting that these ABCB1s may also serve as BR transporters (Figure 4E).

We next compared the BL-binding site in ABCB1 with the structure of the human bile acid exporter ABCB11 (hABCB11) bound with taurocholate (Wang et al., 2022). Structure alignment revealed a similar fold of the TMD and NBD, with an RMSD of 2.7 Å of 1013 Cα pairs (Supplemental Figure 9B). The BL-binding site in ABCB1 merged well with the taurocholate site, with the ligands adopting a similar orientation (Supplemental Figure 9B). In both structures, the steroidal rings of the substrate packed to the hydrophobic cavity surface (Supplemental Figure 9B and 9C). Whereas the polymethyl and polyhydroxyl tail of BL protruded into a hydrophobic pocket in ABCB1, the negatively charged taurine ring of taurocholate was stabilized by a tyrosine residue, Y145, in hABCB11 (Wang et al., 2022) (Supplemental Figure 9B and 9C).

Structural changes in ABCB1 upon BR binding

All determined ABCB1 structures exhibited an inward-facing conformation (Figure 5A). Alignments of the substrate-unbound and BL-bound ABCB1 structures revealed an RMSD of 1.4 Å (Figure 5A). Overall, the two halves of the transporter moved closer upon BL binding, for both the TMDs and NBDs (Figure 5A). In the TMDs, large shifts were observed in TM4, TM9, TM10, and TM12, especially for TM10 and TM12 (Figure 5B). In comparison, such conformational changes upon BL binding were not observed in the ABCB19 structures (Ying et al., 2024). BL binding triggered a conformational change in TM12, particularly at the joint region to the cytosolic part (Figure 5C and 5D). Regions of TM10 and TM12 where large shifts occurred were adjacent to the BL molecule (Figure 5D). Specifically, M967 and V971 in TM12 were involved in

formation of the hydrophobic pocket to accommodate the polymethyl tail of BL (Figures 3A, 5C and 5D). As the conformation changed, E978 in TM12, which interacted with K864 in TM10, rotated away and was no longer in contact with K864 (Figure 5D). As shown in the ATPase assay, the E978A mutant had increased basal ATPase activity in the absence of BL, ~four-fold higher than that of ABCB1^{WT}, whereas the V_{max} value was comparable (Supplemental Figure 8C and 8E). A proline residue (P984) was situated at the joint region of TM12, where large conformational changes occurred (Figure 5D). The P984A mutant also had increased basal ATPase activity, ~eight-fold higher than that of ABCB1^{WT}, as well as a higher V_{max} (Supplemental Figure 8C and 8E). However, the E978A and P984A mutants had a BL transport ability similar to that of ABCB1^{WT} in the proteoliposome-based transport assay (Supplemental Figure 8A). The roles of these two residues in BR transport remain to be fully characterized. The conformational changes in the TMDs of ABCB1 were transferred to the NBDs mainly through four short inter-TM helices (ICHs) positioned between the TMDs and NBDs. ICH1 between TM2 and TM3 and ICH4 between TM10 and TM11 mediated the interactions between TMD1 and NBD1, and ICH2 between TM4 and TM5 and ICH3 between TM8 and TM9 mediated the interactions between TMD2 and NBD2 (Supplemental Figure 9D). Extensive interactions were formed between the ICHs and the corresponding NBDs, including both hydrophobic or ionic interactions and hydrogen bonding (Supplemental Figure 9D). Such ICH motifs are conserved in the determined structures of the ABCB family and other ABC transporter families, playing essential roles in coupling the movements of the TMDs and NBDs (Alam and Locher, 2023).

In ABC transporters, ATP binding typically triggers closure of NBDs and conformational changes in TMDs (Thomas and Tampé, 2020). However, in the ATP plus BL-bound structure of ABCB1^{EQ}, we did not observe large changes in either NBDs or TMDs. Structure alignments revealed that the ATP plus BL-bound structure of ABCB1 was similar to that of the BL-bound state, with an RMSD of 0.6 Å (Supplemental Figure 9E). ATP binding induced local changes, particularly in NBD1, through interactions between the ATP molecule and the surrounding residues (Supplemental Figure 9F and 9G), but it did not cause the expected closure of the NBDs.

DISCUSSION

Our findings show that, like ABCB19, ABCB1 also functions as a BR exporter in *Arabidopsis*. Although the two BR exporters have similar functions and their BL-binding pockets show some conservation, they may be regulated differently. ABCB1 lacked the R domain that was identified in ABCB19 (Ying et al., 2024), and the linker sequence in ABCB1 corresponding to the R domain of ABCB19 shared a low sequence identity (Supplemental Figure 1). The R domain plays an inhibitory role in the activity of ABCB19 (Ying et al., 2024). Consistent with its lack of an R domain, ABCB1 had higher ATPase activity than ABCB19 in the presence and absence of BL (Figure 1C and 1D), although this was not positively correlated with its ability to transport CSA in *Arabidopsis* protoplasts (Supplemental Figure 3A and 3B). Although only bioactive BRs, not auxin, triggered the ATPase activities of ABCB1 and ABCB19 *in vitro*, both transporters have previously been characterized as auxin transporters (Noh et al., 2001, 2003; Geisler et al., 2005; Lin and Wang, 2005; Lewis et al., 2007; Hao et al., 2020). Therefore, an intriguing question is how ABCB1 and ABCB19 transport these two distinct phytohormones. The transport activity of ABCB1 has been reported to be regulated by the AGC protein kinase PINOID (PID) through phosphorylation of its linker sequence (Henrichs et al., 2012). S634 was identified as a possible residue phosphorylated by PID, and an S634E mutation increased the auxin export activity of ABCB1 (Henrichs et al., 2012). Whether this residue plays a role in BR transport requires further study.

ABCB1 and ABCB19 show overlapping as well as distinct expression patterns in different plant tissues and growth stages, contributing to redundant or synergistic functions (Noh et al., 2001; Geisler et al., 2005; Cecchetti et al., 2015). For example, whereas *ABCB19* is highly expressed in the inflorescence stem or seedling hypocotyl, *ABCB1* expression is not detected in these cells (Noh et al., 2001). Consistent with these observations, the *abcb1* mutant shows no visible phenotypes, whereas the *abcb19* mutant is defective in the growth of these organs (Noh et al., 2001). Both *ABCB1* and *ABCB19* are involved in floral development. However, the floral phenotype is apparent only in the *abcb1 abcb19* double mutant, suggesting functional redundancy of the two transporters (Noh et al., 2001). In addition, *ABCB1* and *ABCB19* have been shown to act redundantly in the regulation of stamen elongation, whereas *ABCB1* contributes mainly to anther development (Noh et al., 2001; Cecchetti et al., 2015). The contribution of BR transport to these plant tissues or growth stages remains to be studied.

The apo state, BL-bound, and ATP plus BL-bound structures of ABCB1 were all determined in the inward-facing conformation. The ABCB1^{WT} or ABCB1^{EQ} structures were also solved under different experimental conditions. For example, the ABCB1^{WT} structure was solved in the presence of ATP and BL; in the presence of ATP, ADP, and BL; in the presence of ADP and vanadate; and in the presence of BL and the non-hydrolysable ATP analog AMP-PNP, or ATP-γS (Supplemental Figure 11A). The ABCB1^{EQ} structure was solved in the presence of ATP, ADP, and BL (Supplemental Figure 11A). However, all ABCB1 structures exhibited the same inward-facing conformation according to the EM maps (Supplemental Figure 11A). The dominant inward-facing state captured for both ABCB1 and ABCB19 (Ying et al., 2024) and the failure to capture conformational transitions may be due to difficulty in overcoming the energy barrier for the purified protein or to the absence of some factors involved in regulating the activity of ABCB1 and ABCB19. Using AlphaFold3 (Abramson et al., 2024), we predicted the structure of *Arabidopsis* ABCB1 bound to ATP molecules. The predicted model displayed a distinct conformation compared with the inward-facing structures determined via cryo-EM (Supplemental Figure 11B). The ATP-bound structure has been determined for human ABCB1 (hABCB1), which was in an outward-facing conformation (Kim and Chen, 2018; Alam et al., 2019). The predicted *Arabidopsis* ABCB1 model closely resembled the ATP-bound structure of hABCB1, with an RMSD of 1.9 Å (Supplemental Figure 11D) (Kim and Chen, 2018). However, the substrate-binding cavity of the predicted structure remained closed on the extracellular side, exhibiting an occluded conformation (Supplemental Figure 11C). Structure alignments

between the predicted model and the inward-facing structure of *Arabidopsis* ABCB1 determined in the presence of BL revealed an RMSD of 9.0 Å (Supplemental Figure 11E). Large conformational changes were observed in both the NBDs and the TMDs (Supplemental Figure 11E). Upon ATP binding, the two NBDs moved closer and interacted in a head-to-tail manner, a conserved feature of ABC transporters (Supplemental Figure 11F) (Kim and Chen, 2018; Thomas and Tampé, 2020). Structural shifts in the NBDs were relayed to the TMDs via the ICHs that connected the TMDs and NBDs, leading to conformational changes within the TMDs (Supplemental Figures 9D and 11G). Structure alignments of the TMDs in the predicted model and the inward-facing structure revealed that the transmembrane segments in the first half of the TMDs, including TM1–TM3, TM6, and TM11, remained relatively unchanged. By contrast, the remaining transmembrane segments (TMs) underwent significant rearrangements (Supplemental Figure 11G). On the cytosolic side, the two TMD halves moved closer, closing off the substrate-binding cavity, while, on the extracellular side, TMs of the second half, such as TM4–TM5 and TM7–TM8, rotated to widen the opening of the cavity (Supplemental Figure 11G). These conformational changes are consistent with those observed in the structural transitions of other ABCB transporters, such as hABCB1 (Kim and Chen, 2018; Thomas and Tampé, 2020). However, we noticed that a helix located between the two halves of *Arabidopsis* ABCB1 (residues 595–615), a part of the linker sequence that may be implicated in regulation of transport activity via phosphorylation, underwent a significant shift during the transition between the inward-facing and occluded conformations (Supplemental Figure 11B). In the inward-facing structure, this linker was positioned between the two NBDs, potentially inhibiting their closure (Supplemental Figure 11B). In the occluded structure model, the helix shifted downward, allowing the two NBDs to come together (Supplemental Figure 11B). Notably, this helix is not conserved in hABCB1 structures (Supplemental Figures 1 and 11D). Whether this helix contributes to the dominant inward-facing conformation of *Arabidopsis* ABCB1 captured in cryo-EM and its role in regulating BR transport remain to be clarified. Nonetheless, the functional and structural characterizations of ABCB19 (Ying et al., 2024) and ABCB1 presented here provide a basis for re-examining the substrate specificity of the transporters and their roles in the cross-talk between auxin and BRs in plants.

METHODS

Plant material and growth conditions

A. thaliana (L.) Heynh., accession Columbia-0 (Col-0), was used in all experiments. Seeds were surface sterilized with sterilization buffer (80% [v/v] ethanol, 2.5% [v/v] sodium hypochlorite), stratified for 2 days in the dark at 4°C, and grown vertically on half-strength Murashige and Skoog 1% (w/v) agar plates supplemented with 1% (w/v) sucrose at 22°C with a 16-h/8-h light/dark photoperiod. The following mutants and transgenic *Arabidopsis* lines have been described previously (Ying et al., 2024): *p35S:ABCB1-GFP*/Col-0 (ABCB1OE, T3-3–5), *abcb1-100* (SALK_083649), and the *abcb1 abcb19* double mutant generated by crossing *abcb1-100* with *abcb19-101* (SALK_033455).

Chemical treatments

The BL (OlChemIm), IAA (Sigma-Aldrich), IBA (Sigma-Aldrich), GA3 (Sigma-Aldrich), campesterol (MedChemExpress), 24-epiBL (Solarbio), 24-epiCS (MedChemExpress), taurocholic acid (MedChemExpress), cholesterol (Sigma-Aldrich), and estrone sulfate (Aladdin) used in this study are commercially available. The 22-OHCR and CSA were custom made (Wang et al., 2023), kept at different stock concentrations in DMSO (Sigma-Aldrich), and diluted 1000× to reach final concentrations in the media. The BL, 24-epiBL, 24-epiCS, 22-OHCR, GA3, campesterol, taurocholic acid, estrone sulfate, IAA, and IBA used for measurements were dissolved in DMSO at a concentration of 100 mM, pre-diluted to different concentrations, and added to the reaction mixture to ensure the same content of DMSO (1%, v/v). Cholesterol (Sigma-Aldrich) was dissolved in ethyl alcohol at a concentration of 100 mM, pre-diluted to different concentrations, and added to the reaction mixture to ensure the same content of ethyl alcohol (0.5%, v/v).

Plasmid construction

The full-length *Arabidopsis ABCB1* (At2G36910) and *TWD1* (AT3G21640) genes were amplified from an *A. thaliana* cDNA library. To generate the *ABCB1* mutants, site-directed mutagenesis was performed with a standard two-step PCR. The sequence fragments of *ABCB1* (wild type and mutants) and *TWD1* were subcloned into the *pCAG* vector with a C-terminal FLAG tag (DYKDDDDK) plus His_8 tag and a His_8 tag, respectively. All constructs were verified by DNA sequencing. The *p35S:ABCB1-GFP* and *p35S:ABCB19-GFP* constructs used for transient expression in protoplasts were generated by Golden Gate assembly (New England Biolabs). PCR was used to amplify the full-length genomic coding regions of *ABCB1* (AT2G36910) and *ABCB19* (AT3G28860) (from ATG to the last codon before the STOP codon), and the BsaI restriction sites were removed using site-directed mutagenesis. The *ABCB1(Y286A)*, *ABCB1(Y941A)*, *ABCB1(Y286AY941A)*, and *ABCB1(E532QE1188Q)* point mutations were generated in g*ABCB1* by site-directed mutagenesis with PCR-driven overlap extension. The resulting genomic DNA fragments were cloned into the *pGGC000* entry vector (Lampropoulos et al., 2013) and recombined together with the entry clones containing the *35S* promoter and *GFP* (C-terminal fusion) into the final expression vector *pGG_AG_KmR* using a protocol described previously (Decaestecker et al., 2019). The *p35S:GFP-ABCG25* expression construct was described previously (Ying et al., 2024). Primers are listed in Supplemental Table 3.

Protein expression and purification

HEK293F cells (Sino Biological) were cultured in SMM 293T-II medium (M293TII, Sino Biological) at 37°C and 130 rpm under 5% CO_2 and transfected upon reaching a density of 2×10^6 cells per ml. A total of 1.5 mg of plasmids of *ABCB1* and *TWD1* at a ratio of 2:1 were pre-incubated with 4 mg of linear polyethylenimines (Polysciences) in 45 ml of medium for 15 min. The mixture was then added to 800 ml of HEK293F cells, followed by a static incubation for 15 min. After a 12-h transfection, 10 mM sodium butyrate (Sigma-Aldrich) was added to the cells, and they were cultured for an additional 48 h at 30°C. The transfected cells were harvested by centrifugation at 2100 *g* for 10 min, and the cell pellets were resuspended in lysis buffer containing 25 mM HEPES–KOH (pH 7.4) and 150 mM NaCl, to which protease inhibitor cocktail (1 mM PMSF, 1.3 μg ml^{-1} aprotinin, 0.7 μg ml^{-1} pepstatin A, and 5 μg ml^{-1} leupeptin) and 1.5% (w/v) dodecyl maltopyranoside (DDM, Anatrace) were added. After incubation in a rotating shaker at 4°C for 2 h, the mixture was centrifuged at 200 000 *g* for 60 min. The supernatant was isolated and incubated with anti-FLAG M2 affinity resin (Sigma-Aldrich) at 4°C for 40 min.

For cryo-EM sample preparation, the resin was rinsed three times using lysis buffer plus 0.06% (w/v) digitonin (Apollo Scientific) and then eluted using lysis buffer supplemented with 0.06% (w/v) digitonin (Apollo Scientific) and 200 μg ml^{-1} FLAG peptide. The protein eluent was concentrated to 2 ml using a 100-kDa cutoff Centricon filter (Millipore) and further purified by size-exclusion chromatography (Superose-6 Increase, 10/300 GL, GE Healthcare) in lysis buffer plus 0.03% (w/v) digitonin. Peak fractions

were collected and concentrated to about 10 mg ml^{-1} for cryo-EM sample preparation.

For the ATPase activity assay and proteoliposome reconstitution, the protein was expressed and purified in the same way, except that the detergent used in the wash and elution buffer on the affinity columns was substituted with 0.02% (w/v) DDM, and the detergent used in the buffer for size-exclusion chromatography was substituted with 0.01% (w/v) DDM. Peak fractions were collected and concentrated to about 2 mg ml^{-1}.

ATPase activity assay

The ATPase activities of *Arabidopsis* ABCB1^{WT} and its mutants were measured by quantifying inorganic phosphate using the ATPase Colorimetric Assay Kit (Innova Biosciences) in 96-well plates. To measure ATPase activity against different substrates, 3 μg of protein was incubated with different substrates for 10 min on ice in reaction buffer containing 25 mM HEPES–KOH (pH 7.4), 150 mM KCl, 10 mM $MgCl_2$, and 0.01% (w/v) DDM. The reaction was initiated by the addition of ATP at a final concentration of 3 mM and then incubated at 37°C for 10 min. The reaction was terminated by addition of 25 μl malachite development solution and incubated for 2 min at room temperature prior to adding 10 μl of 10% oxalic acid. The amount of released inorganic phosphate was measured by light absorbance at a wavelength of 650 nm with a BioTek Synergy H1 Multimode Reader. Statistical analysis was performed using GraphPad Prism 8, and the kinetics of ABCB1 ATPase activities with serial concentrations of ligands were fitted to the Hill equation.

Proteoliposome reconstitution

Proteoliposomes were prepared as described previously (Geertsma et al., 2008; Ying et al., 2024). In brief, soybean phospholipids (Sigma-Aldrich) were dried twice with nitrogen gas after dissolving in a methanol:chloroform 3:1 (v/v) (Sigma-Aldrich) mixture and pentane (Sigma-Aldrich) at 50 mg ml^{-1}. Reconstitution buffer containing 20 mM HEPES–KOH (pH 7.4), 150 mM KCl, and 2 mM EDTA was used to resuspend the lipids at a concentration of 20 mg ml^{-1}. Lipids were then frozen and thawed 10 times in liquid nitrogen. For reconstitution, liposomes were extruded through 0.4-μm membrane filters (Cytiva) 31 times and incubated with 1% DDM for 1 h at 4°C. Protein purified in DDM was added to the lipid mixture at a ratio of 1:100 (w/w) and then incubated for 1 h at 4°C. Biobeads (Bio-Rad) were added at 100 mg ml^{-1} in four batches to remove the detergent. After removal of Biobeads, the liposomes were further homogenized by five freeze-thaw cycles and then extruded 10 times. Proteoliposomes were collected by ultracentrifugation at 160 000 *g* for 1 h and resuspended in transport buffer containing 20 mM HEPES–KOH (pH 7.4) and 150 mM KCl to a final concentration of 100 mg ml^{-1}.

[^{3}H]-BL transport assay

The proteoliposome-based transport assay was performed using a rapid filtration method (Geertsma et al., 2008; Kuromori et al., 2010; Ying et al., 2024). In brief, the reaction was initiated by addition of 2 μl proteoliposomes to 48 μl reaction buffer containing 20 mM HEPES–KOH (pH 7.4), 150 mM KCl, 2 mM ATP, 1 μM BL, 7 nM [^{3}H]-BL (specific activity 0.6 Ci mmol^{-1}, American Radiolabeled Chemicals), and 5 mM $MgCl_2$ at room temperature. For the control group, 1 mM sodium orthovanadate (Med Chem Express) or 1 mM EDTA was added to the reaction buffer. Transport was stopped by transferring the samples to glass fiber filters (0.3 mm, Advantec). The filters were then washed rapidly with 8 ml of ice-cold buffer containing 20 mM HEPES–KOH (pH 7.4) and 150 mM KCl. The filters were incubated with 3 ml of scintillation solution for 2 h, and the radioactivity was measured by liquid scintillation counting (Tri-Carb 2910TR, PerkinElmer). For the time-course assay, the accumulation of [^{3}H]-BL at different time points was calculated relative to the mean amount measured at 0 min. For the ABCB1 mutants, BL accumulation at 45 min was calculated as the difference between the experimental group and the control group.

Transport assay in *Arabidopsis* protoplasts

For the transport assay, protoplasts were isolated from 4-week-old rosette leaves of wild-type *Arabidopsis* (Col-0), *abcb1* and *abcb1 abcb19* mutants, and *p35S:ABCB1-GFP*/Col-0 (ABCB1-OE) as described previously (Ying et al., 2024). In brief, the leaf epidermal surface was removed using a "tape–*Arabidopsis* sandwich" method (Wu et al., 2009) and transferred to a Petri dish containing 20 ml of enzyme solution (0.5 M sucrose, 10 mM MES–KOH [pH 5.7], 20 mM $CaCl_2$, 40 mM KCl, 1% [w/v] cellulase Onozuka R10 [Yakult, Tokyo, Japan], and 1% [w/v] Macerozyme Onozuka R10 [Yakult]). The leaves were incubated in the dark for 2 h, and the released protoplasts were collected by centrifugation at 600 *g* for 4 min. Protoplasts were washed with and resuspended in 10 ml of W5 solution (0.1% [w/v] glucose, 0.08% [w/v] KCl, 0.9% [w/v] NaCl, 1.84% [w/v] $CaCl_2$, and 2 mM MES–KOH [pH5.7]) and kept in the dark overnight before being used for DNA transfection or directly for transport assays. Plasmids containing *p35S:ABCB1-GFP*, *p35S:ABCB1(Y286A)-GFP*, *p35S:ABCB1(Y941A)-GFP*, *p35S:ABCB1(Y286AY941A)-GFP*, *p35S:ABCB1(E532QE1188Q)-GFP*, *p35S:ABCB19-GFP*, and *p35S:ABCG25-GFP* were introduced into protoplasts isolated from *Arabidopsis* Col-0 by PEG-mediated transfection. The transfected protoplasts were incubated in W5 solution overnight. Protoplasts were divided into three equal portions from each genotype after isolation and transfection, then incubated separately in W5 solution containing 10 μM CSA (two portions) or DMSO (mock, one portion) for 4 h (feeding process). After feeding, protoplasts were washed briefly with W5 solution to remove excess CSA. DMSO-treated and one portion of the CSA-treated protoplasts were fixed immediately with 3.7% (v/v) formaldehyde (Sigma-Aldrich) in W5 for 15 min, washed three times with wash buffer (3% [w/v] bovine serum albumin in W5), and kept in dark conditions for a click reaction. The other portion of CSA-treated protoplasts was transferred to fresh W5 solution and incubated for 4 h (export process), then fixed and washed the same way as the other two portions. The fixed protoplasts were followed by click reactions using the Click-&-Go Cell Reaction Buffer Kit (Click Chemistry Tools, cat. no. 1263) and azide-BDP-FL (Jena Bioscience; cat. no. CLK-044-1) at a final concentration of 3 μM in the reaction mixture for 40 min. Samples were washed three times with wash buffer and imaged.

Microscopy and image analysis

All images were obtained using an SP8X confocal microscope (Leica) with an X40/0.75 water immersion objective. GFP was excited at 488 nm and imaged at 500–530 nm. The BDP-FL signal was excited at 503 nm and captured with a 505–519-nm emission filter. Images were analyzed with Fiji software.

Cryo-EM sample preparation

For ABCB1$^{WT\ in\ the}$ substrate-unbound state, samples were prepared using the Vitrobot Mark IV (Thermo Fisher Scientific). In brief, a 4-μl protein aliquot was applied to a holey carbon grid (Quantifoil Cu R1.2/1.3, 300 mesh) glow discharged by SOLARUS 950 Plasma Cleaner (Gatan) using H_2 and O_2 for 10 s. The grid was blotted with grade 597 Filter Paper (Cytiva Whatman) for 3 s at 8°C and 100% humidity. The grid was then plunged into liquid ethane precooled by liquid nitrogen and transferred to a storage box. For BL-bound ABCB1^{WT} and the ATP plus BL-bound ABCB1^{EQ} mutant, each 4-μl protein aliquot was incubated with 1 mM BL, or 1 mM BL, 5 mM ATP, and 5 mM $MgCl_2$ on ice for 30 min before cryo-EM sample preparation.

Cryo-EM data collection and processing

All data were collected with EPU software in super-resolution mode on a 300-kV Titan Krios microscope (Thermo Fisher Scientific) equipped with a K3 Summit direct electron detector (Gatan) and a GIF Quantum energy filter (Gatan) at a nominal magnification of 81 000× with defocus values ranging from −1.0 to −2.0 μm and a calibrated pixel size of 0.55 Å. Each movie stack was acquired with an exposure time of 3 s and dose-fractioned into 32 frames, yielding a total accumulated dose of 50 e^- Å^{-2}. Data were then imported into RELION 4.0, motion corrected,

and dose weighted with MotionCor2 (Zheng et al., 2017; Zivanov et al., 2018). The resulting micrographs were binned two-fold, yielding a pixel size of 1.1 Å, and then imported into cryoSPARC (v.3.2.0) (Punjani et al., 2017). The defocus values of each image were determined using CTFFIND4 (Rohou and Grigorieff, 2015). Data processing for substrate-unbound ABCB1^{WT}, BL-bound ABCB1^{WT}, and ATP plus BL-bound ABCB1^{EQ} followed a similar scheme, and a detailed procedure for substrate-unbound ABCB1 is described below as an example. Detailed flowcharts for all data processing can be found in Supplemental Figures 5A, 6A, and 7A.

For substrate-unbound ABCB1^{WT}, 3660 micrograph stacks were collected. 3 839 205 particles were automatically picked by the template picker in cryoSPARC and then applied to multiple rounds of 2D classification. 1 755 837 particles were selected and subjected to *ab initio* reconstruction with five classes. C1 symmetry was applied during the entire process. 265 131 particles were selected for non-uniform refinement. An EM map at 4.7 Å was obtained with clear structural features and served as a reference for further heterogeneous refinement. After several rounds of heterogeneous refinement and *ab initio* reconstruction, 288 714 particles were selected for non-uniform refinement, finally yielding a reconstruction map at 3.5 Å resolution.

The overall resolution of the final maps of substrate-unbound ABCB1^{WT}, BL-bound ABCB1^{WT}, and ATP plus BL-bound ABCB1^{EQ} were determined by the gold-standard Fourier shell correlation at a 0.143 criterion (Chen et al., 2013), and the local resolutions were estimated using implements in cryoSPARC.

Model building and refinement

The apo-state structure model of *A. thaliana* ABCB1 predicted by AlphaFold2 was docked into the obtained cryo-EM density maps using UCSF Chimera (Pettersen et al., 2004; Jumper et al., 2021). The fitted structures were manually adjusted in Coot (Emsley and Cowtan, 2004). Further refinements were performed using phenix.real_space_refine in PHENIX (Adams et al., 2010). The BL molecule was built and refined using restraints generated by Elbow (Adams et al., 2010). Statistics for the 3D reconstruction and model refinement can be found in Supplemental Table 1. An ATP-bound structure model of *A. thaliana* ABCB1 was predicted using AlphaFold3 (Abramson et al., 2024). All structural figures were prepared with PyMol or UCSF Chimera software.

Statistical analysis

Data were analyzed with GraphPad Prism 8. Significance of differences was determined using unpaired two-tailed *t*-tests or one-way ANOVA with Dunnett's or Tukey's multiple comparison test. The sample sizes were chosen to ensure the reproducibility of the experiments and to obtain meaningful results.

DATA AND CODE AVAILABILITY

The ABCB1 structures in the substrate-unbound state, BL-bound state, and ATP plus BL-bound state have been deposited in the Protein Data Bank under accession codes 8ZPX, 8ZPZ, and 8ZQ4, respectively. The corresponding cryo-EM density maps have been deposited in the Electron Microscopy Data Bank under accession codes EMD-60366, EMD-60369, and EMD-60370, respectively.

FUNDING

This work was supported by the National Natural Science Foundation of China (grants 32322041 and 32321001 to L.S., grant 32471279 to X.L.); the Strategic Priority Research Program of the Chinese Academy of Sciences (grant XDB37020103 to L.S.); Research Funds of the Center for Advanced Interdisciplinary Science and Biomedicine of IHM (grant QYPY20230034 to L.S.); the Natural Science Foundation of Anhui Province (grant 2408085JX005 to L.S.); Fundamental Research Funds for the Central Universities (grant WK9100000031 to L.S.); USTC Research Funds of the Double First-Class Initiative (grant YD9100002004 to L.S. and grant YD9100002020 to X.L.); Research Foundation Flanders (grant G002121N to E.R.); and the Chinese Scholarship Council predoctoral fellowships (H.Z.).

ACKNOWLEDGMENTS

We thank the Cryo-EM Center of the University of Science and Technology of China for the EM facility support. We thank Yaowei Wang, Yongming Luo, and Nemanja Vukašinović (VIB-UGhent, Belgium) for useful discussions and technical support. L.S. is supported by an Outstanding Young Scholar Award from the Qiu Shi Science and Technologies Foundation and a Young Scholar Award from the Cyrus Tang Foundation. No conflict of interest is declared.

AUTHOR CONTRIBUTIONS

L.S., E.R., X.L., and S.T. conceived the idea and the project design. H.W., W.Y., Y.G., X.L., and L.S. contributed the biochemical and structural work. X.L. and L.S. designed experiments and analyzed data. H.W. and W.Y. performed most of the molecular cloning, protein purification, ATPase and transport assays, and structure determination work. W.Y. and Y.G. performed the cryo-EM data collection. H.Z., Q.M., and E.R. contributed the work in *Arabidopsis*. H.Z. performed most of the experiments in *Arabidopsis*. H.J., M.K., and J.M.W. synthetized CSA and 22-OHCR. H.W., E.R., X.L., and L.S. wrote the manuscript. All authors reviewed and approved the final manuscript.

SUPPLEMENTAL INFORMATION

Supplemental information is available at *Plant Communications Online*.

Received: June 20, 2024
Revised: September 18, 2024
Accepted: October 31, 2024
Published: November 4, 2024

REFERENCES

Abramson, J., Adler, J., Dunger, J., Evans, R., Green, T., Pritzel, A., Ronneberger, O., Willmore, L., Ballard, A.J., Bambrick, J., et al. (2024). Accurate structure prediction of biomolecular interactions with AlphaFold 3. Nature **630**:493–500. https://doi.org/10.1038/s41586-024-07487-w.

Adams, P.D., Afonine, P.V., Bunkóczi, G., Chen, V.B., Davis, I.W., Echols, N., Headd, J.J., Hung, L.W., Kapral, G.J., Grosse-Kunstleve, R.W., et al. (2010). PHENIX: a comprehensive Python-based system for macromolecular structure solution. Acta Crystallogr. D Biol. Crystallogr. **66**:213–221. https://doi.org/10.1107/S0907444909052925.

Alam, A., and Locher, K.P. (2023). Structure and Mechanism of Human ABC Transporters. Annu. Rev. Biophys. **52**:275–300. https://doi.org/10.1146/annurev-biophys-111622-091232.

Alam, A., Kowal, J., Broude, E., Roninson, I., and Locher, K.P. (2019). Structural insight into substrate and inhibitor discrimination by human P-glycoprotein. Science **363**:753–756. https://doi.org/10.1126/science.aav7102.

Atkovska, K., Klingler, J., Oberwinkler, J., Keller, S., and Hub, J.S. (2018). Rationalizing Steroid Interactions with Lipid Membranes: Conformations, Partitioning, and Kinetics. ACS Cent. Sci. **4**:1155–1165. https://doi.org/10.1021/acscentsci.8b00332.

Bailly, A., Sovero, V., Vincenzetti, V., Santelia, D., Bartnik, D., Koenig, B.W., Mancuso, S., Martinoia, E., and Geisler, M. (2008). Modulation of P-glycoproteins by auxin transport inhibitors is mediated by interaction with immunophilins. J. Biol. Chem. **283**:21817–21826. https://doi.org/10.1074/jbc.M709655200.

Bouchard, R., Bailly, A., Blakeslee, J.J., Oehring, S.C., Vincenzetti, V., Lee, O.R., Paponov, I., Palme, K., Mancuso, S., Murphy, A.S., et al. (2006). Immunophilin-like TWISTED DWARF1 modulates auxin efflux

activities of *Arabidopsis* P-glycoproteins. J. Biol. Chem. **281**:30603–30612. https://doi.org/10.1074/jbc.M604604200.

Cecchetti, V., Brunetti, P., Napoli, N., Fattorini, L., Altamura, M.M., Costantino, P., and Cardarelli, M. (2015). ABCB1 and ABCB19 auxin transporters have synergistic effects on early and late *Arabidopsis* anther development. J. Integr. Plant Biol. **57**:1089–1098. https://doi.org/10.1111/jipb.12332.

Chen, S., McMullan, G., Faruqi, A.R., Murshudov, G.N., Short, J.M., Scheres, S.H.W., and Henderson, R. (2013). High-resolution noise substitution to measure overfitting and validate resolution in 3D structure determination by single particle electron cryomicroscopy. Ultramicroscopy **135**:24–35. https://doi.org/10.1016/j.ultramic.2013.06.004.

Choe, S., Dilkes, B.P., Fujioka, S., Takatsuto, S., Sakurai, A., and Feldmann, K.A. (1998). The DWF4 gene of Arabidopsis encodes a cytochrome P450 that mediates multiple 22alpha-hydroxylation steps in brassinosteroid biosynthesis. Plant Cell **10**:231–243. https://doi.org/10.1105/tpc.10.2.231.

Decaestecker, W., Buono, R.A., Pfeiffer, M.L., Vangheluwe, N., Jourquin, J., Karimi, M., Van Isterdael, G., Beeckman, T., Nowack, M.K., and Jacobs, T.B. (2019). CRISPR-TSKO: A Technique for Efficient Mutagenesis in Specific Cell Types, Tissues, or Organs in Arabidopsis. Plant Cell **31**:2868–2887. https://doi.org/10.1105/tpc.19.00454.

Dudler, R., and Hertig, C. (1992). Structure of an mdr-Like Gene from Arabidopsis thaliana: Evolutionary implications. J. Biol. Chem. **267**:5882–5888. https://doi.org/10.1016/S0021-9258(18)42636-1.

Emsley, P., and Cowtan, K. (2004). coot: model-building tools for molecular graphics. Acta Crystallogr D Biol Crystallogr. **60**:2126–2132. https://doi.org/10.1107/S0907444904019158.

Fujioka, S., and Yokota, T. (2003). Biosynthesis and metabolism of brassinosteroids. Annu. Rev. Plant Biol. **54**:137–164. https://doi.org/10.1146/annurev.arplant.54.031902.134921.

Geertsma, E.R., Nik Mahmood, N.A.B., Schuurman-Wolters, G.K., and Poolman, B. (2008). Membrane reconstitution of ABC transporters and assays of translocator function. Nat. Protoc. **3**:256–266. https://doi.org/10.1038/nprot.2007.519.

Geisler, M., Blakeslee, J.J., Bouchard, R., Lee, O.R., Vincenzetti, V., Bandyopadhyay, A., Titapiwatanakun, B., Peer, W.A., Bailly, A., Richards, E.L., et al. (2005). Cellular efflux of auxin catalyzed by the Arabidopsis MDR/PGP transporter AtPGP1. Plant J. **44**:179–194. https://doi.org/10.1111/j.1365-313X.2005.02519.x.

Hao, P., Xia, J., Liu, J., Di Donato, M., Pakula, K., Bailly, A., Jasinski, M., and Geisler, M. (2020). Auxin-transporting ABC transporters are defined by a conserved D/E-P motif regulated by a prolylisomerase. J. Biol. Chem. **295**:13094–13105. https://doi.org/10.1074/jbc.RA120.014104.

Henrichs, S., Wang, B., Fukao, Y., Zhu, J., Charrier, L., Bailly, A., Oehring, S.C., Linnert, M., Weiwad, M., Endler, A., et al. (2012). Regulation of ABCB1/PGP1-catalysed auxin transport by linker phosphorylation. EMBO J. **31**:2965–2980. https://doi.org/10.1038/emboj.2012.120.

Hothorn, M., Belkhadir, Y., Dreux, M., Dabi, T., Noel, J.P., Wilson, I.A., and Chory, J. (2011). Structural basis of steroid hormone perception by the receptor kinase BRI1. Nature **474**:467–471. https://doi.org/10.1038/nature10153.

Huang, X., Zhang, X., An, N., Zhang, M., Ma, M., Yang, Y., Jing, L., Wang, Y., Chen, Z., and Zhang, P. (2023). Cryo-EM structure and molecular mechanism of abscisic acid transporter ABCG25. Nat. Plants **9**:1709–1719. https://doi.org/10.1038/s41477-023-01509-7.

Jumper, J., Evans, R., Pritzel, A., Green, T., Figurnov, M., Ronneberger, O., Tunyasuvunakool, K., Bates, R., Žídek, A., Potapenko, A., et al. (2021). Highly accurate protein structure prediction with AlphaFold. Nature **596**:583–589. https://doi.org/10.1038/s41586-021-03819-2.

Kim, H.B., Kwon, M., Ryu, H., Fujioka, S., Takatsuto, S., Yoshida, S., An, C.S., Lee, I., Hwang, I., and Choe, S. (2006). The regulation of DWARF4 expression is likely a critical mechanism in maintaining the homeostasis of bioactive brassinosteroids in Arabidopsis. Plant Physiol. **140**:548–557. https://doi.org/10.1104/pp.105.067918.

Kim, Y., and Chen, J. (2018). Molecular structure of human P-glycoprotein in the ATP-bound, outward-facing conformation. Science **359**:915–919. https://doi.org/10.1126/science.aar7389.

Kuromori, T., Miyaji, T., Yabuuchi, H., Shimizu, H., Sugimoto, E., Kamiya, A., Moriyama, Y., and Shinozaki, K. (2010). ABC transporter AtABCG25 is involved in abscisic acid transport and responses. Proc Natl Acad Sci USA **107**:2361–2366. https://doi.org/10.1073/pnas.0912516107.

Lampropoulos, A., Sutikovic, Z., Wenzl, C., Maegele, I., Lohmann, J.U., and Forner, J. (2013). GreenGate - A Novel, Versatile, and Efficient Cloning System for Plant Transgenesis. PLoS One **8**:e83043. https://doi.org/10.1371/journal.pone.0083043.

Lewis, D.R., Miller, N.D., Splitt, B.L., Wu, G., and Spalding, E.P. (2007). Separating the roles of acropetal and basipetal auxin transport on gravitropism with mutations in two ABC transporter genes. Plant Cell **19**:1838–1850. https://doi.org/10.1105/tpc.107.051599.

Lin, R., and Wang, H. (2005). Two homologous ATP-binding cassette transporter proteins, AtMDR1 and AtPGP1, regulate Arabidopsis photomorphogenesis and root development by mediating polar auxin transport. Plant Physiol. **138**:949–964. https://doi.org/10.1104/pp.105.061572.

Noh, B., Murphy, A.S., and Spalding, E.P. (2001). Multidrug resistance-like genes of Arabidopsis required for auxin transport and auxin-mediated development. Plant Cell **13**:2441–2454. https://doi.org/10.1105/tpc.13.11.2441.

Noh, B., Bandyopadhyay, A., Peer, W.A., Spalding, E.P., and Murphy, A.S. (2003). Enhanced gravi- and phototropism in plant *mdr* mutants mislocalizing the auxin efflux protein PIN1. Nature **423**:999–1002. https://doi.org/10.1038/nature01716.

Nolan, T.M., Vukašinović, N., Liu, D., Russinova, E., and Yin, Y. (2020). Brassinosteroids: Multidimensional Regulators of Plant Growth, Development, and Stress Responses. Plant Cell **32**:295–318. https://doi.org/10.1105/tpc.19.00335.

Northey, J.G.B., Liang, S., Jamshed, M., Deb, S., Foo, E., Reid, J.B., McCourt, P., and Samuel, M.A. (2016). Farnesylation mediates brassinosteroid biosynthesis to regulate abscisic acid responses. Nat. Plants **2**:16114. https://doi.org/10.1038/Nplants.2016.114.

Pettersen, E.F., Goddard, T.D., Huang, C.C., Couch, G.S., Greenblatt, D.M., Meng, E.C., and Ferrin, T.E. (2004). UCSF chimera - A visualization system for exploratory research and analysis. J. Comput. Chem. **25**:1605–1612. https://doi.org/10.1002/jcc.20084.

Punjani, A., Rubinstein, J.L., Fleet, D.J., and Brubaker, M.A. (2017). cryoSPARC: algorithms for rapid unsupervised cryo-EM structure determination. Nat. Methods **14**:290–296. https://doi.org/10.1038/Nmeth.4169.

Rea, P.A. (2007). Plant ATP-Binding cassette transporters. Annu. Rev. Plant Biol. **58**:347–375. https://doi.org/10.1146/annurev.arplant.57.032905.105406.

Rohou, A., and Grigorieff, N. (2015). CTFFIND4: Fast and accurate defocus estimation from electron micrographs. J. Struct. Biol. **192**:216–221. https://doi.org/10.1016/j.jsb.2015.08.008.

Sánchez-Fernández, R., Davies, T.G., Coleman, J.O., and Rea, P.A. (2001). The Arabidopsis thaliana ABC protein superfamily, a

complete inventory. J. Biol. Chem. **276**:30231–30244. https://doi.org/10.1074/jbc.M103104200.

Santiago, J., Henzler, C., and Hothorn, M. (2013). Molecular mechanism for plant steroid receptor activation by somatic embryogenesis co-receptor kinases. Science **341**:889–892. https://doi.org/10.1126/science.1242468.

She, J., Han, Z., Kim, T.W., Wang, J., Cheng, W., Chang, J., Shi, S., Wang, J., Yang, M., Wang, Z.Y., and Chai, J. (2011). Structural insight into brassinosteroid perception by BRI1. Nature **474**:472–476. https://doi.org/10.1038/nature10178.

Sun, Y., Han, Z., Tang, J., Hu, Z., Chai, C., Zhou, B., and Chai, J. (2013). Structure reveals that BAK1 as a co-receptor recognizes the BRI1-bound brassinolide. Cell Res. **23**:1326–1329. https://doi.org/10.1038/cr.2013.131.

Symons, G.M., and Reid, J.B. (2004). Brassinosteroids do not undergo long-distance transport in pea. Implications for the regulation of endogenous brassinosteroid levels. Plant Physiol. **135**:2196–2206. https://doi.org/10.1104/pp.104.043034.

Thomas, C., and Tampé, R. (2020). Structural and Mechanistic Principles of ABC Transporters. Annu. Rev. Biochem. **89**:605–636. https://doi.org/10.1146/annurev-biochem-011520-105201.

Thomas, C., Aller, S.G., Beis, K., Carpenter, E.P., Chang, G., Chen, L., Dassa, E., Dean, M., Duong Van Hoa, F., Ekiert, D., et al. (2020). Structural and functional diversity calls for a new classification of ABC transporters. FEBS Lett. **594**:3767–3775. https://doi.org/10.1002/1873-3468.13935.

Vukasinovic, N., and Russinova, E. (2018). BRexit: Possible Brassinosteroid Export and Transport Routes. Trends Plant Sci. **23**:285–292. https://doi.org/10.1016/j.tplants.2018.01.005.

Vukasinovic, N., Wang, Y.W., Vanhoutte, I., Fendrych, M., Guo, B.Y., Kvasnica, M., Jiroutová, P., Oklestkova, J., Strnad, M., and Russinova, E. (2021). Local brassinosteroid biosynthesis enables optimal root growth. Nat. Plants **7**:619–632. https://doi.org/10.1038/s41477-021-00917-x.

Wang, L., Hou, W.T., Wang, J., Xu, D., Guo, C., Sun, L., Ruan, K., Zhou, C.Z., and Chen, Y. (2022). Structures of human bile acid exporter ABCB11 reveal a transport mechanism facilitated by two tandem substrate-binding pockets. Cell Res. **32**:501–504. https://doi.org/10.1038/s41422-021-00611-9.

Wang, Y., Perez-Sancho, J., Platre, M.P., Callebaut, B., Smokvarska, M., Ferrer, K., Luo, Y., Nolan, T.M., Sato, T., Busch, W., et al. (2023). Plasmodesmata mediate cell-to-cell transport of brassinosteroid hormones. Nat. Chem. Biol. **19**:1331–1341. https://doi.org/10.1038/s41589-023-01346-x.

Wu, F.H., Shen, S.C., Lee, L.Y., Lee, S.H., Chan, M.T., and Lin, C.S. (2009). Tape-Arabidopsis Sandwich - a simpler Arabidopsis protoplast isolation method. Plant Methods **5**:16. https://doi.org/10.1186/1746-4811-5-16.

Wu, G., Otegui, M.S., and Spalding, E.P. (2010). The ER-Localized TWD1 Immunophilin Is Necessary for Localization of Multidrug Resistance-Like Proteins Required for Polar Auxin Transport in Arabidopsis Roots. Plant Cell **22**:3295–3304. https://doi.org/10.1105/tpc.110.078360.

Ye, L., Liu, L., Xing, A., and Kang, D. (2013). Characterization of a dwarf mutant allele of Arabidopsis MDR-like ABC transporter AtPGP1 gene. Biochem Biophys Res Commun. **441**:782–786. https://doi.org/10.1016/j.bbrc.2013.10.136.

Yin, Y., Wang, Z.Y., Mora-Garcia, S., Li, J., Yoshida, S., Asami, T., and Chory, J. (2002). BES1 accumulates in the nucleus in response to brassinosteroids to regulate gene expression and promote stem elongation. Cell **109**:181–191. https://doi.org/10.1016/s0092-8674(02)00721-3.

Ying, W., Liao, L., Wei, H., Gao, Y., Liu, X., and Sun, L. (2023). Structural basis for abscisic acid efflux mediated by ABCG25 in *Arabidopsis thaliana*. Nat. Plants **9**:1697–1708. https://doi.org/10.1038/s41477-023-01510-0.

Ying, W., Wang, Y., Wei, H., Luo, Y., Ma, Q., Zhu, H., Janssens, H., Vukašinović, N., Kvasnica, M., Winne, J.M., et al. (2024). Structure and function of the *Arabidopsis* ABC transporter ABCB19 in brassinosteroid export. Science **383**:eadj4591. https://doi.org/10.1126/science.adj4591.

Zheng, S.Q., Palovcak, E., Armache, J.P., Verba, K.A., Cheng, Y., and Agard, D.A. (2017). MotionCor2: anisotropic correction of beam-induced motion for improved cryo-electron microscopy. Nat. Methods **14**:331–332. https://doi.org/10.1038/nmeth.4193.

Zivanov, J., Nakane, T., Forsberg, B.O., Kimanius, D., Hagen, W.J., Lindahl, E., and Scheres, S.H. (2018). New tools for automated high-resolution cryo-EM structure determination in RELION-3. Elife **7**:e42166. https://doi.org/10.7554/eLife.42166.